Titanium oxide improves boron nitride photocatalytic degradation of perfluorooctanoic acid

Lijie Duan [a,b,c,d,1], Bo Wang [c,d,1], Kimberly N. Heck [a,d,1], Chelsea A. Clark [c,d], Jinshan Wei [a,b], Minghao Wang [a,b], Jordin Metz [d,e], Gang Wu [f], Ah-Lim Tsai [f], Sujin Guo [d,g], Jacob Arredondo [c], Aditya D. Mohite [c,i], Thomas P. Senftle [c,d], Paul Westerhoff [d,h], Pedro Alvarez [c,d,e,i], Xianghua Wen [b], Yonghui Song [a,b,*], Michael S. Wong [c,d,e,g,i,*]

[a] State Key Laboratory of Environmental Criteria and Risk Assessment, Chinese Research, Academy of Environmental Sciences, Beijing, China
[b] School of Environment, Tsinghua University, Beijing, China
[c] Department of Chemical and Biomolecular Engineering, Rice University, Houston, TX, USA
[d] Center for Nanotechnology Enabled Water Treatment, Rice University, Houston, TX, USA
[e] Department of Chemistry, Rice University, Houston, TX, USA
[f] Department of Internal Medicine, University of Texas-McGovern Medical School at Houston, Houston, TX, USA
[g] Department of Environmental Engineering, Rice University, Houston, TX, USA
[h] School of Sustainable Engineering and Built Environment, Arizona State University, Tempe, AZ, USA
[i] Department of Materials Science and NanoEngineering, Rice University, Houston, TX, USA

ABSTRACT

Boron nitride (BN) has the newly-found property of degrading recalcitrant polyfluoroalkyl substances (PFAS) under ultraviolet C (UV-C, 254 nm) irradiation. It is ineffective at longer wavelengths, though. In this study, we report the simple calcination of BN and UV-A active titanium oxide (TiO_2) creates a BN/TiO_2 composite that is more photocatalytically active than BN or TiO_2 under UV-A for perfluorooctanoic acid (PFOA). Under UV-A, BN/TiO_2 degraded PFOA $\sim 15 \times$ faster than TiO_2, while BN was inactive. Band diagram analysis and photocurrent response measurements indicated that BN/TiO_2 is a type-II heterojunction semiconductor, facilitating charge carrier separation. Additional experiments confirmed the importance of photogenerated holes for degrading PFOA. Outdoor experimentation under natural sunlight found BN/TiO_2 to degrade PFOA in deionized water and salt-containing water with a half-life of 1.7 h and 4.5 h, respectively. These identified photocatalytic properties of BN/TiO_2 highlight the potential for the light-driven destruction of other PFAS.

1. Introduction

Per- and polyfluoroalkyl substances (PFAS), a class of anthropogenic persistent chemicals, have been extensively used to manufacture industrial and consumer products [1]. The most common PFAS are perfluorooctanoic acid (PFOA) and perfluorooctanesulfonate (PFOS) [2]. Due to the stable C-F bonds (485 kJ/mol), PFOA has half-lives of 3 years in human blood, ~250 years in ocean water, and even longer in soil [3]. PFOA has adverse health outcomes, such as reproductive toxicity, nephrotoxicity, neurotoxicity, and carcinogenicity [4], and parts-per-billion (μg/L) levels of PFOA have been detected in human tissues. PFAS pollution is omnipresent, and these compounds are found in the atmosphere, [5] rainwater [6], and drinking water sources [7]. There are growing reports of PFAS occurring not only in developing countries [8] but also in the Middle East and Asia [9,10] as well as in remote Arctic waters [11]. The major known sources of PFASs in the environment include aqueous film-forming foam [12], landfill leachate [13], and wastewater discharges from manufacturing facilities [14,15]. Notably, PFAS has been detected in acidic wastewaters, *e.g.,* from perfluorooctanesulfonyl fluoride production (pH ~ 4) [16], and semiconductor [17], chromium plating, and photolithographic wastewaters (pH ~ 3) [18]. While there are currently no PFAS limits for industrial wastewaters, the US EPA initiated plans to set wastewater discharge standards [19], necessitating more effective PFAS removal.

Photocatalysts have been shown effective for PFOA degradation with relatively lower energy requirements than existing methods [20,21]. Compositions of catalysts have included TiO_2 materials [22–24], Bi-based materials [25–28], as well as SiC[29], Ga_2O_3[30], and In_2O_3 [31,32]. Many of these materials require complex syntheses and have not been scaled up, which make near-term adaptation unlikely. We recently reported that BN photodegrades PFOA, PFOS, and Gen-X under UV-C [33,34]. While BN has been used in many commercial products (*e. g.*, cosmetics, coatings, and lubricants [35]), BN had not been previously regarded as photocatalytically active. Formally considered a wide-band gap semiconductor material ($E_g \sim 5.8$ eV) [36], we found that BN can absorb 254-nm light (photon energy ~ 4.8 eV) due to mid-gap states introduced by internal and/or edge defects. Upon illumination, the photoexcited holes (h^+) and generated reactive oxygen species (ROS) contribute to PFOA oxidation.

To expand the PFAS photocatalytic capabilities of BN, we postulated that a composite material containing both BN and TiO_2 could be photocatalytically active at illumination wavelengths (*i.e.*, UV-A, 315–400 nm) longer than UV-C (250–280 nm). UV-A is present in sunlight [37] which intimates a solar-based remediation strategy. UV-A is advantageous over UV-C, since this wavelength is absorbed less by naturally occurring organics (*e.g.*, humic acids) in real waters [38]. Recent reports have shown the ability of Pt/TiO_2 [23], $BiOI/Bi_5O_7I$ [39], MnO_x/In_2O_3 [40], and other composites to photocatalytically degrade PFOA under UV-A or simulated sunlight (Table S1). BN-containing composites have not been studied for PFAS photocatalysis under UV-A or sunlight yet.

We note that BN/C_3N_4 [41], BN/TiO_2 [42–47] and other BN composites have been studied for the photodegradation of model organic dyes and other environmentally relevant contaminants (*i.e.*, 1,4-dioxane [48] and ibuprofen [49]) under UV-A and visible light (Table S2). In these, BN is thought to function mainly as a hydrophobic support, with the possibility of improving photocatalytic efficiency by lessening e^-/h^+ recombination. However, within these studies, there is disagreement as to whether it is electrons or holes that migrate to the BN, and there was no consideration of BN being a photo-active component. BN-containing composites remain poorly characterized and their band diagrams and photocatalytic mechanisms not well understood. We address some of these issues in this work.

Here, we report the simple synthesis of a BN/TiO_2 composite photocatalyst through the calcination of powdered mixtures composed of commercially available BN and TiO_2 P25. We characterized BN/TiO_2 via transmission electron microscopy (TEM), X-ray powder diffraction (XRD), diffuse reflectance UV–vis spectroscopy (DR-UV), X-ray photoelectron spectroscopy (XPS), and ultraviolet photoelectron spectrometry (UPS). We quantified its activity for PFOA degradation using BN-only and TiO_2-only samples as comparisons. We assessed BN/TiO_2 to be highly effective under UV-A irradiation, which can be rationalized using a band diagram model constructed for the semiconductor composite. We analyzed possible PFOA degradation mechanisms using electron paramagnetic resonance (EPR) spectroscopy and reactive radical species capture experiments. In exploring one way for implementation, we found that BN/TiO_2 photocatalytically degrades PFOA within hours under natural sunlight in simulated water contained in clear plastic water bottles.

2. Experimental

2.1. Materials

Perfluorooctanoic acid (PFOA, $C_7F_{15}COOH$, 96% purity), perfluoroheptanoic acid (PFHpA, $C_6F_{13}COOH$, 99% purity), perfluorohexanoic acid (PFHxA, $C_5F_{11}COOH$, 98% purity), perfluoropentanoic acid (PFPeA, C_4F_9COOH, 98% purity), perfluorobutanoic acid (PFBA, C_3F_7COOH, 99% purity), pentafluoropropionic acid (PFPrA, C_2F_5COOH, 98% purity), trifluoroacetic acid (TFA, CF_3COOH, 99% purity), *tert*-butanol (TBA, 99% purity),

superoxide dismutase (SOD, 3000 units/mg protein), ethylenediaminetetraacetate disodium salt dihydrate (EDTA-2Na, 99% purity), hexagonal- boron nitride (BN, powder, ~ 1 µm, 98% purity), titanium dioxide (TiO_2, nano-powder, ~21 nm particle size, 99.5%, P25, 80 wt% anatase and 20 wt% rutile phases) were obtained from Sigma-Aldrich, 5-*tert*-butoxycarbonyl-5-methyl-1-pyrroline-N-oxide (BMPO) ($\geq$99.9% purity) was obtained from Enzo Life Sciences. Unless otherwise indicated, the water used in all experiments was deionized (DI) water (18.2 MΩ).

2.2. Methods

2.2.1. Synthesis of BN/TiO_2 composite materials

Powders of BN (400 mg, ball-milled for 15 min to increase surface defect content [33]) and TiO_2 were mixed in 20 mL of water. The TiO_2 amount was chosen such that the weight ratio of BN:TiO_2 (x:y) varied from 5:1 to 1:3. The pH of the mixture was in the range of 3.9–5.7, which promoted the electrostatic attraction of TiO_2 (isoelectric point $pH_{IEP} \sim$ 6.5) and BN ($pH_{IEP} \sim 2.8$) particles in suspension. After 1 h of stirring, the mixture was heated until dry. The white-colored powder was calcined at 600 °C for 2 h under air to promote covalent adhesion at the BN/TiO_2 interface. After assessing photocatalytic activity for all BN/TiO_2(x:y) samples, we determined that the weight ratio of 1:1 showed maximum photoactivity (Figures S1 and S2, Supporting Information). We focused this study on BN/TiO_2(1:1) (hereafter termed "BN/TiO_2"). Accounting for their molar mass (80 g/mol for TiO_2 and 25 g/mol for BN) and density differences (4.2 g/cm^3 for TiO_2 and 2.1 g/cm^3 for BN), BN/TiO_2 can be estimated to contain 24 mol% TiO_2 or 33 vol% TiO_2.

2.2.2. Characterization of photocatalysts

The crystalline structures of the photocatalysts were characterized using XRD. The phase and crystal morphology of the photocatalysts were obtained by TEM images with a JEOL 2010 TEM operating at an accelerating voltage of 200 kV. The elemental composition and the bond configuration of the photocatalysts were obtained by using XPS equipped with a PHI Quantera System. The obtained spectra were corrected using the C 1 s peak at 284.6 eV. Particle sizes, shapes, and compositions of BN, TiO_2, and BN/TiO_2 composite materials were determined by a scanning electron microscope (SEM) with energy-dispersive X-ray (EDS) (JEOL JSM-6500F, Japan). Multipoint nitrogen physisorption was performed on the samples following 5 h under vacuum at 150 °C and the specific surface areas were determined by Brunauer–Emmett–Teller (BET) theory (Table S3). Band positions were determined using UPS using a PHI5000 VersaProbe III (Scanning ESCA Microprobe) equipped with a spherical analyzer and He UV source. The absorption spectra of the photocatalysts were measured using DR-UV, where the powders were diluted with 60 wt% of $BaSO_4$, pressed into wafers, and measured using a Shimadzu UV-2450 spectrometer. The photoelectrochemical performance was tested by an electrochemical workstation (CHI 760E) with a traditional three-electrode system [50] (see Text S1 for details).

2.2.3. Photocatalysis treatment procedures

Photocatalytic reactions were conducted in an enclosed, for safety, photoreactor UV system identical with our previously work [33], equipped with six UV-C Ushio G4T5 low pressure mercury lamps (input: 4 W; output: 0.8 W) for the 254 nm UV-C experiments, or six 4 W (input) UV-A Sunlite F4T5 fluorescent lamps (input: 4 W; output: 0.8 W) for the 365 nm UV-A experiments (see text S2 for details).

2.2.4. Analytical methods

The PFOA concentration was measured via high-performance liquid chromatography (HPLC, 1260 Infinity II Agilent, USA) with an Agilent WPH C18 column (4.6 mm × 250 mm, 5 µm) and the short-chain byproducts were quantified via HPLC-MS (Agilent 1200 HPLC equipped with MicroToF mass spectrometry, detection limit of 0.01 mg/L), as done previously [33] (see Text S3).

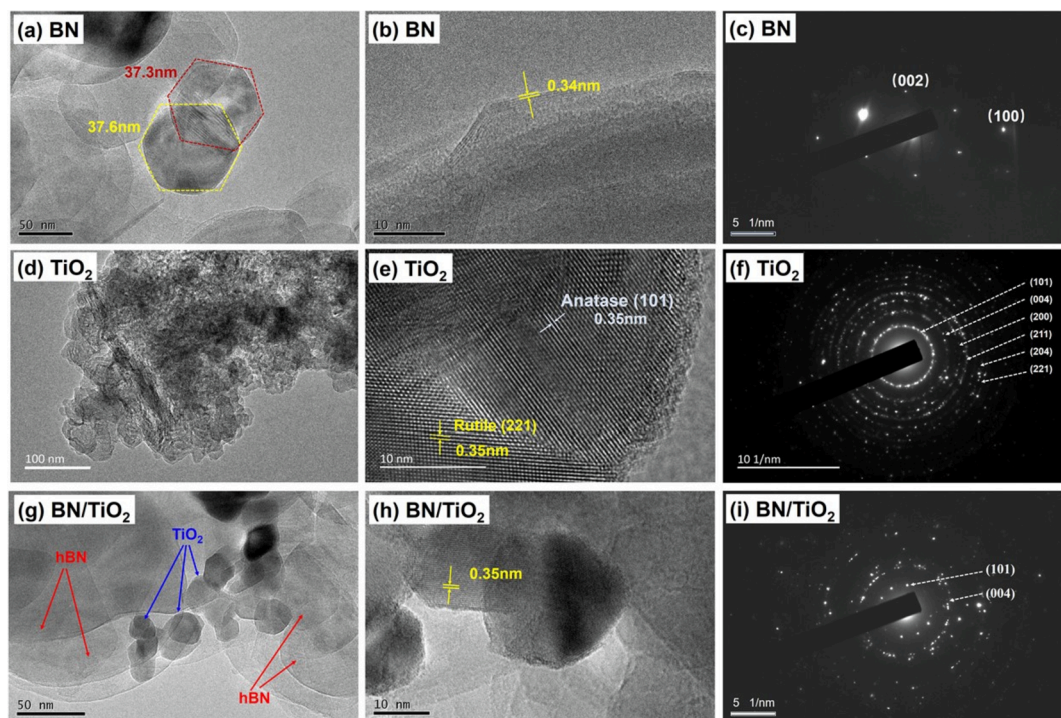EPR spectroscopy measurements were performed using a Bruker

Fig. 1. HRTEM images of (a,b) BN (c, SAED pattern), (d,e) TiO₂ (f, SAED pattern), and (g, h) BN/TiO₂ (i, SAED pattern).

EMX spectrometer. Experiments were conducted in a 4-mL quartz cuvette with a stir bar, adding a pH-adjusted catalyst slurry, 1000 mg/L BMPO (spin-trapping agent), and any radical scavenging agents (3 mM EDTA-2Na or 100 mM TBA), for a final solution volume of 1-mL. This was placed in the UV reactor described above, for 5 min of irradiation. Aliquots of reaction mixture were transferred into capillary tubes for EPR measurements. EPR measurements were conducted at room temperature, with a frequency of 9.32 GHz, with 100 kHz modulation frequency, 0.2 – 0.5 G modulation amplitude, 20 mW power, and 163 ms time constant.

All measurements were repeated in triplicate and reported as the average values.

3. Results and discussion

3.1. BN and TiO₂ are well-mixed and interfaced in the calcined BN/TiO₂ composite

The XRD patterns confirmed the crystal structure of the BN, TiO₂, and the composite BN/TiO₂ (Figure S3, Supporting Information). BN displays three diffraction peaks at 2θ = 26.5°, 41.7°, and 55.2°, corresponding to the (0 0 2), (1 0 0), and (0 0 4) facets of the hexagonal phase of BN, respectively [44]. For TiO₂, the diffraction peaks indexed to the anatase and rutile crystalline phases were observed, in good agreement with published data on P25 [51]. BN/TiO₂ showed diffraction peaks of both BN and TiO₂, indicating the crystalline phases of BN and TiO₂ were unchanged following calcination. No diffraction peak at ~ 15° was observed, indicating the absence of B₂O₃ in the BN and BN/TiO2 composite materials.

The detailed morphologies of the materials were investigated by HR-TEM (Fig. 1). For each sample, including BN, TiO₂, and BN/TiO₂ composite, images from 10 + spots were taken by TEM to confirm its morphology. Fig. 1a shows the layered hexagonal morphology of BN and the particle size of BN is ~ 40 nm. The dark grey area in the image is indicative of thick stacks of sheets, while the light grey areas represent a relatively small number of stacked sheets or possibly single sheets. The lattice spacing was 0.34 nm (Fig. 1b), corresponding well with the

literature [52]. The electron diffraction rings correspond to the (0 0 2) and (1 0 0) lattice planes, respectively (Fig. 1c), consistent with XRD results (Figure S3). Fig. 1d shows a mixture of small TiO₂ particles. A lattice spacing of 0.35 nm was observed in Fig. 1e, corresponding to the (1 0 1) and (2 1 1) planes of the anatase and rutile, respectively. From the corresponding selected area electron diffraction (SAED) pattern (Fig. 1f), the diffraction rings were indexed to (1 0 1), (0 0 4), (2 0 0), (2 1 1), (2 0 4), and (2 2 1) facets [53], matching well with the XRD results for TiO₂. HRTEM images (Fig. 1g) of the BN/TiO₂ composite showed that the BN and TiO₂ domains had no obvious change after calcination, and the TiO₂ localized at the BN edges of BN, as supported by elemental mapping (Figure S4c-f, Supporting Information). The weaker signals in the SAED pattern of BN/TiO₂ reflects the dilution of the TiO₂ fraction by BN (i).

Deconvolution of the B 1 s, N 1 s, and O 1 s XPS peaks provided information about the average oxidation state and bonding environment in the BN and BN/TiO₂ catalysts (Fig. 2). For BN, two peaks at 190.7 eV and 191.6 eV are associated with B-N and B-OH bonds, respectively, with the latter indicating the BN contained oxygen, as expected (Fig. 2a). Peak area analysis indicates that most of the B (90 mol%) was bonded to N, with the rest to OH (10%). In addition to these two XPS peaks, BN/TiO₂ exhibited a third peak centered at 192.1 eV, which represents the B 1 s binding energy associated with the B-O-Ti bond, thus confirming the formation of covalently bonded interface between the BN and TiO₂ (Fig. 2b) [43]. Most of the B remained in the B-N form (87 mol %), with 9% and 4% as B-OH and B-O-Ti, respectively. In comparing the BN and BN/TiO₂ materials, the B-OH percentage remained similar, but B-N percentage decreased, suggesting the TiO₂ formed B-O-Ti bonds by rupturing B-N bonds during calcination.

The N 1 s XPS peak for BN and for BN/TiO₂, centered at 398.3 eV, represents N atoms bound to B atoms (Fig. 2c,d). XPS peaks at 398.8 eV [54] and 407.3 eV [55] were not observed, indicating the absence (or below-detection-limit amounts) of N–H and N-O bonds. The O 1 s binding energy peak at 532.6 eV seen for BN and BN/TiO₂ represents the B-OH bond (Fig. 2e,f). The much more intense XPS peaks at 531.8 eV and 534.6 eV represent Ti-O-Ti and Ti-O-B bonding environments in BN/TiO₂ (Fig. 2f) [42,44]. Besides, the BE of the Ti 2p peak redshifted for the
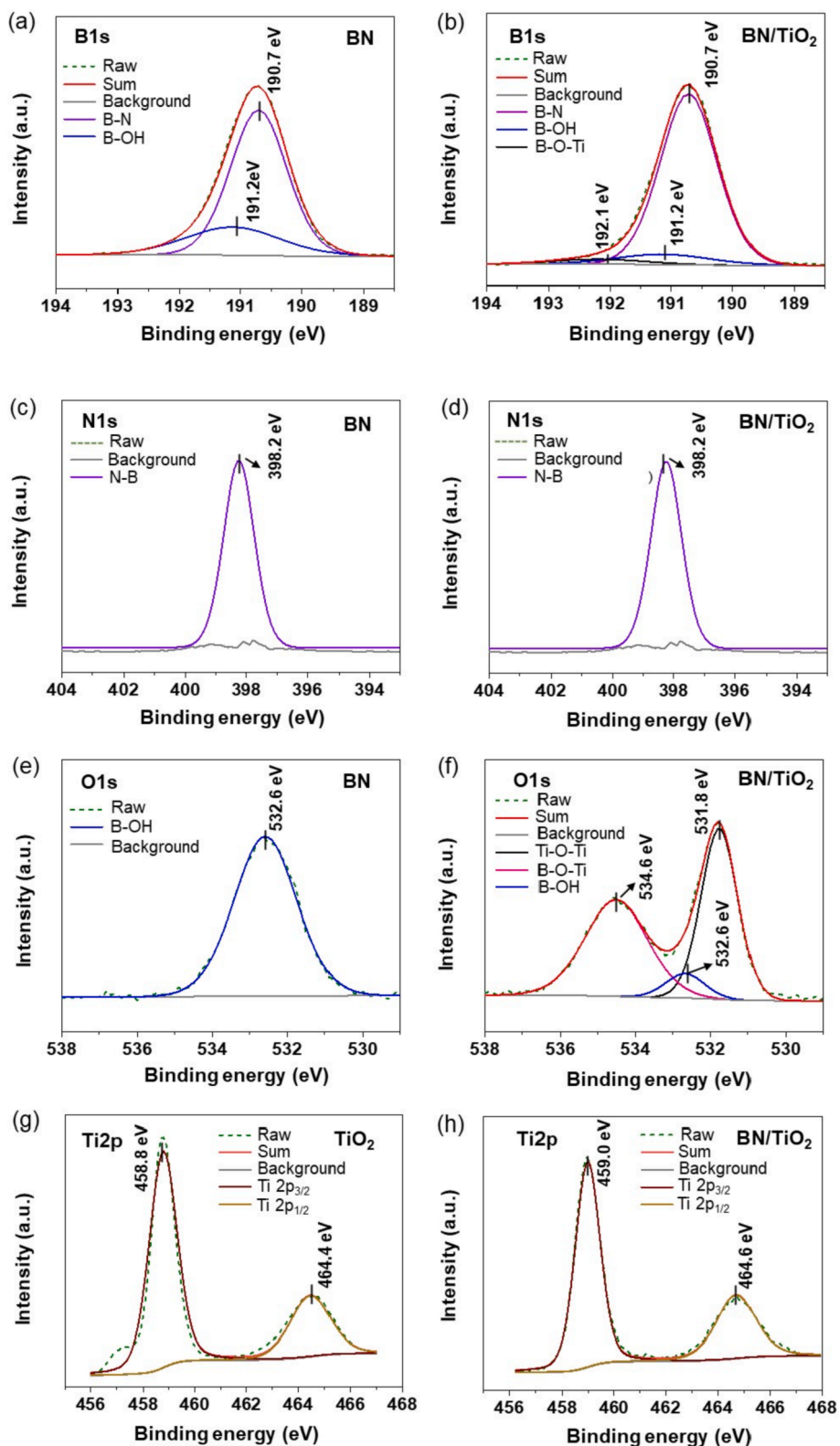
Fig. 2. Deconvolution of XPS spectra: B1s, N1s, O1s, and Ti2p spectra of BN (a, c and e), TiO$_2$ (g), and BN/TiO$_2$ catalysts (b, d, f, and h).

composite (Fig. 2h) compared to TiO$_2$ (Fig. 2g), further supporting the existence of Ti-O-B bond [56]. Peak area analysis indicated that 12%, 44%, and 44% of the O atoms were in B-OH, Ti-O-Ti, and B-O-Ti environments respectively, indicating substantial covalent interfacing between the TiO$_2$ and BN as almost half the oxygens contained in the BN/TiO$_2$ are found as B-O-Ti bonds. No B-O-B bonding (533.4 eV) [57] was

observed, indicating negligible B$_2$O$_3$ present in either BN or BN/TiO$_2$.

3.2. BN/TiO$_2$ is more active than BN or TiO$_2$ for PFOA degradation under UV-A and UV-C

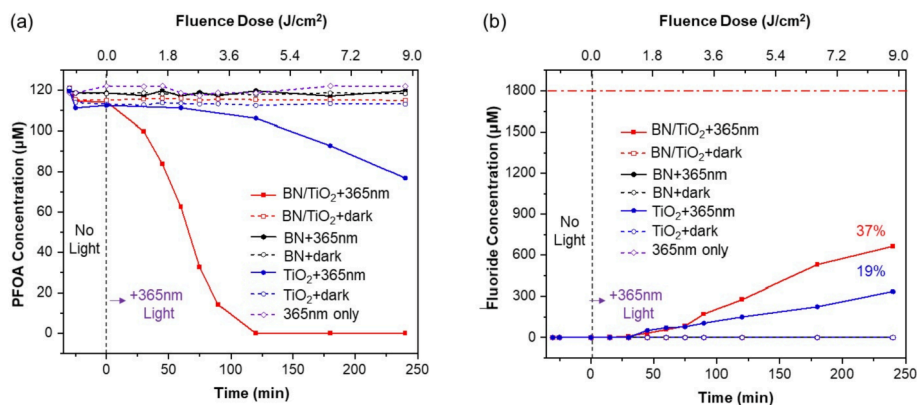We first studied the photocatalytic reaction using UV-A (365-nm)

Fig. 3. (a) HPLC-DAD detected PFOA concentration–time profiles and (b) fluoride concentration profiles using BN, TiO_2, and BN/TiO_2, with and without 365-nm irradiation. Reaction conditions: [PFOA] (at t = -30 min) = ~120 μM (50 ppm), dosage of 0.5 g/L, ambient temperature, air headspace, 365-nm light, photon flux of 1.37×10^{-6} Einstein·L^{-1}·s^{-1}, initial pH = 3.2.
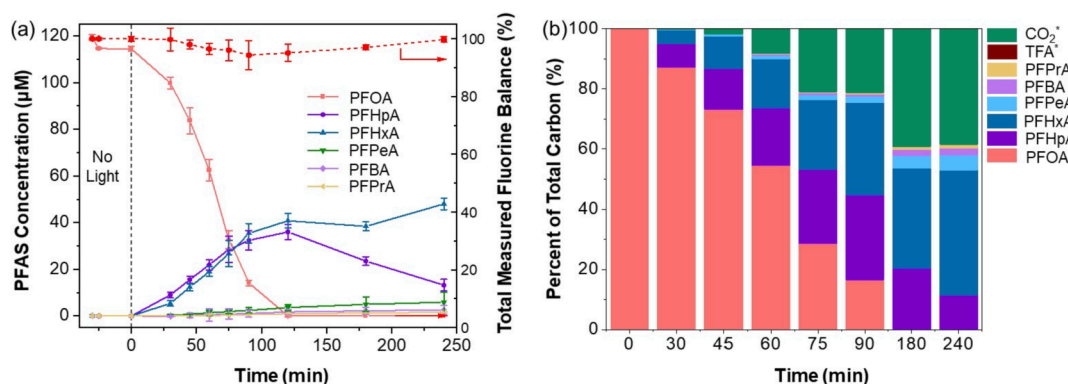

Fig. 4. (a) HPLC-MS detected concentration–time profiles of PFOA and byproducts for the BN/TiO_2 under 365-nm irradiation. (b) Corresponding carbon percentage of PFOA and the byproducts for BN/TiO_2 during the reaction process. Error bars represent the standard deviation of 3 experiments. Reaction conditions: [PFOA] (at t = -30 min) = ~120 μM (50 ppm), dosage of 0.5 g/L, ambient temperature, air headspace, 365-nm light, photon flux of 1.37×10^{-6} Einstein·L^{-1}·s^{-1}, initial pH = 3.2. note: *calculated TFA plus CO_2 carbon percentage for achieving 100% carbon balance.

light (Fig. 3a). BN/TiO_2 and TiO_2 were active, and their optimum dosages were identified (0.5 g/L, Figure S2), while a similar dosage of BN was inactive. PFOA degradation did not occur without illumination or without catalyst (dashed lines, Fig. 3). Prior to initiating photocatalytic experiments, PFOA adsorption on the materials was quantified, with adsorption equilibrium reached within 30 min (initial PFOA concentration of ~ 120 μM decreased by ~ 8%). With BN/TiO_2, the PFOA concentration decreased to < 2.4 μM after 120 min, with a PFOA $t_{1/2}$=55 min. The degradation results exhibit non-uniform kinetics with an induction period happening at the initial 30 min under the light illumination, and the reason will be the subject of a future study. With TiO_2, however, PFOA concentration decreased to 106 μM after 120 min, and 77 μM after 240 min (61% PFOA unreacted); the PFOA had a half-life of ~ 350 min under these conditions. Defluorination was detected, with more fluoride generated with BN/TiO_2 (37%) than with TiO_2 (19%) after 4 h (Fig. 3b).

Because complete mineralization of PFOA was not observed, we quantified the organic degradation byproducts via HPLC-MS, focusing on the BN/TiO_2 system. The main intermediates identified were C_3-C_7 short-chain perfluorinated carboxylic acids (PFCAs) (Fig. 4a). PFHpA (C_7) and PFHxA (C_6) concentrations increased before decreasing, whereas the comparatively lower concentrations of PFPeA (C_5), PFBA (C_4), and PFPrA (C_3) slowly increased with reaction time. These results are consistent with literature [28,31,33,58], where PFOA undergoes step-wise decarboxylation and defluorination to form shortened PFCAs, releasing CO_2 and two F^- ions. Its higher concentrations indicate greater difficulty for C_6 to undergo photodegradation than C_7. Given sufficient

reaction time, the concentrations of shorter-chain PFCAs are expected to reach a maximum before decreasing.

TFA (C_2), a probable decomposition product, was not quantifiable due to interference from residual TFA in the MS background (on the order of ~ 5 μM). Ignoring TFA, we determined the total measured fluorine balance (*i.e.*, the sum of all fluorine in C_3-C_7 PFCAs, unreacted PFOA, and fluoride ions in solution divided by total fluorine of PFOA initially added) was in the range of ~ 93–100%. Assuming the missing fluorine (0–7%) was due to unquantified TFA (which would carry three fluorine atoms), we estimated that there was < 8 μM TFA formed (~7% of starting amount of PFOA).

We assessed the carbon balance by accounting for all carbons in C_3-C_7 PFCAs, unreacted PFOA, and the estimated TFA (8 μM) divided by the total carbon in PFOA initially added (Fig. 4b). We attributed the missing carbon to CO_2, which we did not measure due to experimental difficulties. Our carbon balance indicated the total PFCA content decreased with irradiation time, such that BN/TiO_2 under UV-C converted over one third (38%) of PFOA carbons into CO_2 after 60 min.

We compared BN, TiO_2, and BN/TiO_2 photocatalysis under UV-C (254-nm) illumination also, finding them all active for PFOA degradation (Figure S5). Upon irradiation (t = 0 min), the PFOA concentration–time profiles and half-lives were similar for BN/TiO_2 ($t_{1/2}$=13 min) and BN ($t_{1/2}$=10 min). PFOA degraded more slowly over TiO_2 ($t_{1/2}$=80 min). Non-detectable PFOA concentration levels (~1 ppm = 2.4 μM) were reached after 30 and 45 min for BN/TiO_2 and BN, respectively. Though PFOA degradation rates were similar between the BN/TiO_2 and BN, the composite demonstrated greater defluorination capability with
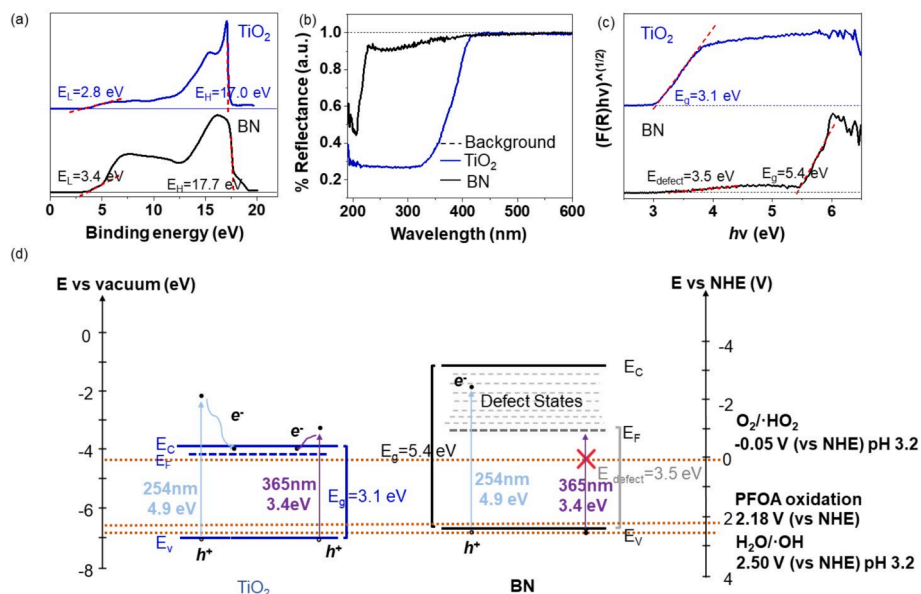
Fig. 5. (a) UP spectra, (b) DR-UV spectra, and (c) Tauc plots for TiO_2 and BN, and (d) corresponding band diagrams with 254 and 365 nm light illumination.

> 50% defluorination reached after 60 min. In comparison, the defluorination was lower with BN (29%) and TiO_2 (7%) after 60 min, indicating that BN/TiO_2 degrades the short-chain byproducts with greater effectiveness. This correlates with the higher CO_2 formation (*i.e.*, greater extent of PFOA mineralization) over BN/TiO_2 (Figure S5), compared to BN or TiO_2 [33].

3.3. BN/TiO_2 is a type-II semiconductor heterojunction with improved charge carrier separation

To better understand the wavelength-dependent photoexcitation and enhanced photocatalytic activity of the BN/TiO_2 composite, we constructed band diagrams for TiO_2 and BN through experimental measurements using UPS and DR-UV. Fig. 5a shows the UPS of TiO_2 and BN, in which the low kinetic energy cutoff (E_L) and high kinetic energy cutoff (E_H) values were determined from the corresponding tangent lines. The
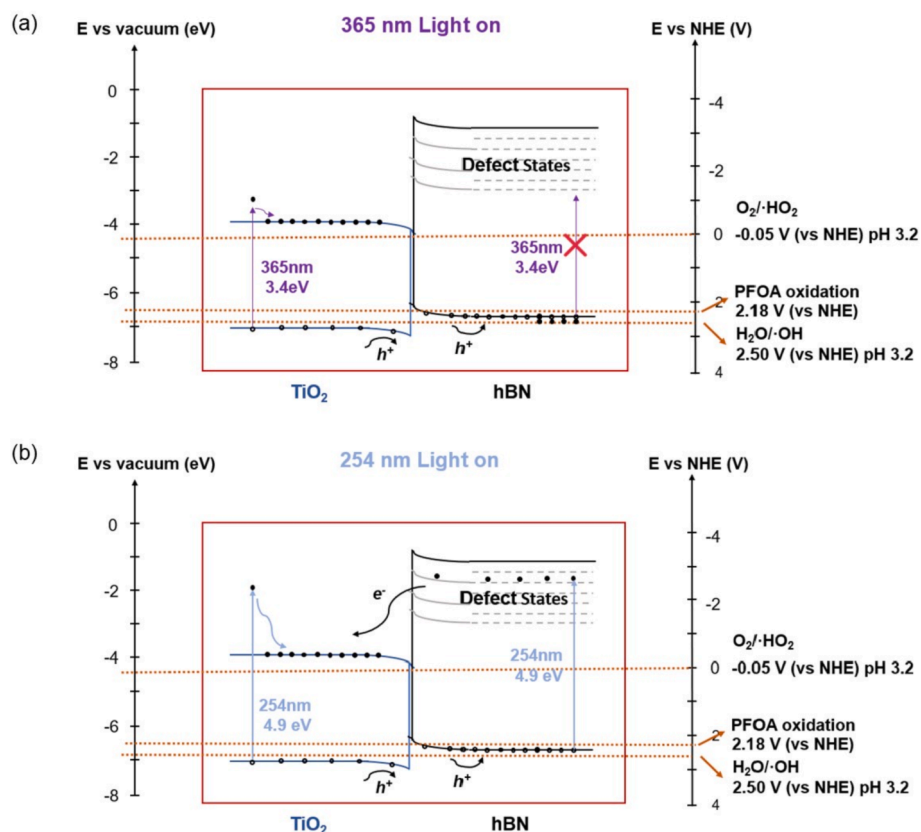

Fig. 6. Proposed band diagram to explain photoexcitation and charge carrier separation mechanism under (a) 365-nm and (b) 254-nm light illumination of BN/TiO_2.
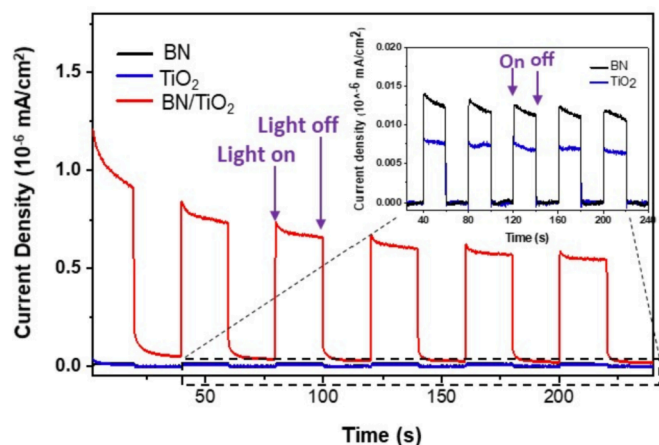
Fig. 7. Photocurrent responses of BN, TiO$_2$ and BN/TiO$_2$ by using light wavelengths ranging from 320 to 500 nm.

Fermi and valence band (VB) levels of TiO$_2$ and BN (versus vacuum) were calculated by the following equations [59]:

$$E_{VBM} = E_H - E_L - h\nu \tag{1}$$

$$E_F = E_L + E_{VBM} \tag{2}$$

where $h\nu$ is the incident photon energy (He I source) of 21.22 eV in UPS. The calculated VB of TiO$_2$ and BN were −7.0 and −6.9 eV (comparable to one another), and the Fermi levels were −4.2 and −3.5 eV, respectively. The DR-UV spectra (Fig. 5b) showed that TiO$_2$ had a broad reflectance throughout the UV region, while BN had a main peak at 208 nm with a tail extending from 220 to 350 nm, consistent with our previous work and attributed to structural defects [33].

Bandgap (E_g) energies were calculated through Tauc analysis (($F(R)$ $h\nu)^{1/2}$ vs $h\nu$) accounting for the indirect bandgap nature of both TiO$_2$ and BN [36,60] (Fig. 5c, Text S4). The bandgap energies of TiO$_2$ and BN were 3.1 eV and 5.4 eV, respectively. The conduction band (CB) level of TiO$_2$ and BN was then calculated by subtracting the bandgap from the VB level.

The TiO$_2$ band diagram matches literature [61], and the band diagram for BN powders was determined experimentally for the first time to our knowledge (Fig. 5d). The redox potentials of the reactive oxygen species (ROS) and PFOA at pH 3.2 are also shown [62,63]. TiO$_2$ is photoexcited and the photogenerated electrons jump to the CB leaving holes at its VB by both 254-nm and 365-nm light since its bandgap is smaller than the respective photon energies (4.9 eV and 3.4 eV). The defects in BN allow photoexcitation at energies > 3.5 eV, which explains why 254-nm light led to photocatalytic activity, but 365-nm irradiation did not.

In the BN/TiO$_2$ composite, charge carrier separation happened at the interface. Comparing the Fermi levels of BN and TiO$_2$ with their optical bandgaps, we conclude that both TiO$_2$ and BN are n-type
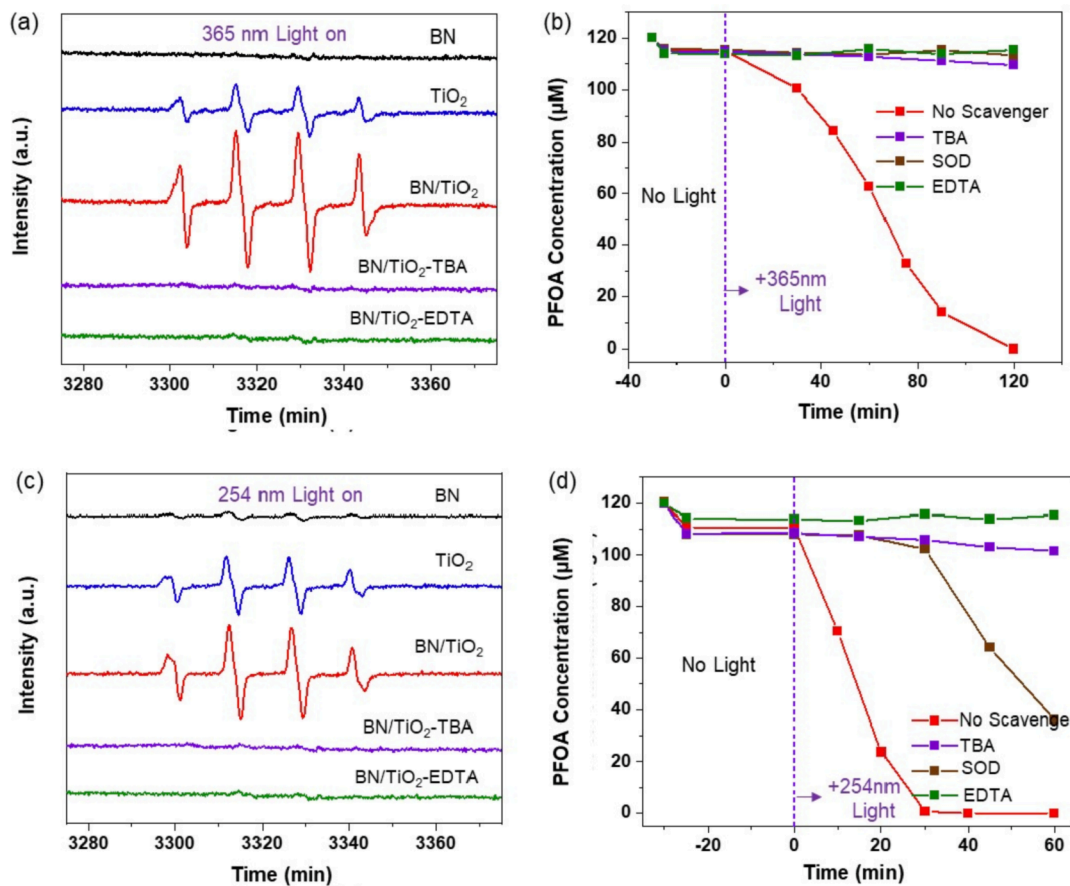

Fig. 8. (a) BMPO spin-trapping EPR spectra of BN, TiO$_2$, and BN/TiO$_2$ under 365-nm light illumination, (b) PFOA photodegradation over BN/TiO$_2$ using EDTA-2Na, SOD and TBA, as hole, superoxide/hydroperoxyl and hydroxyl radical scavengers, respectively under 365-nm light. (c) BMPO spin-trapping EPR spectra of BN, TiO$_2$, and BN/TiO$_2$ under 254-nm light illumination, (d) PFOA photodegradation over BN/TiO$_2$ using EDTA-2Na, SOD and TBA, as hole, superoxide/hydroperoxyl and hydroxyl radical scavengers, respectively under 254-nm light. Reaction conditions: [PFOA]$_0$ = 120 μM, pH = 3.2, scavenging agent concentration = 3 mM (EDTA-2Na), 150 kU/L (SOD), or 100 mM (TBA), BN/TiO$_2$ dosage of 0.5 g/L (under 365-nm) or 1.25 g/L (under 254-nm), ambient temperature, air headspace, 365-nm light with photon flux of 1.37 × 10^{-6} Einstein·L^{-1}·s^{-1}, 254-nm light with photon flux of 6.5 × 10^{-6} Einstein·L^{-1}·s^{-1}.

semiconductors since their Fermi levels are closer to their CB than their VB. Thus, the BN/TiO_2 composite is a type II n-n heterojunction with a staggered structure as illustrated in Fig. 6 [64,65].

When BN/TiO_2 is irradiated with 365 nm light, only the TiO_2 domain with its smaller band gap is photo-excited to generate electrons and holes, which can migrate to more energetically favorable levels via charge transfer [64]. Based on the band diagram, holes from the TiO_2 migrate to BN, and electrons remain in the TiO_2 (Fig. 6a), leading to a net charge separation across the BN/TiO_2 interface. When BN/TiO_2 is irradiated with 254-nm light, a similar charge transfer occurs (Fig. 6b). However, due to the higher energy of the UV-C light, both BN and TiO_2 domains are photoexcited, and the holes migrate to the BN while the photogenerated electrons move to the TiO_2 side.

To provide further evidence for this mechanism, we measured the transient photocurrent response of BN, TiO_2, and BN/TiO_2 to 320–500 nm light (Fig. 7). The current densities decreased after the first 4 cycles, which may be due to surface contamination during preparation [66], but stabilized after 200 s at which point we obtained the steady-state photocurrent. A higher photocurrent implies higher electron-hole separation [67]. The photocurrent value of the BN ($0.012nA/cm^2$) was slightly higher than that of TiO_2 ($0.008nA/cm^2$, Fig. 7 inset), implying that BN has a slower recombination rate, possibly due to the surface defect states. Notably, the steady-state current density of BN/TiO_2 obtained after the stabilization period was $0.56nA/cm^2$, which was $\sim 47 \times$ and $\sim 70 \times$ higher than that of BN and TiO_2, respectively, which implies that the composite has an improved charge separation and lower recombination rate, consistent with our band diagram analysis.

3.4. Photogenerated holes play an important role in BN/TiO_2 photodegradation of PFOA

Comparison of the band positions with the redox potentials for the ROS species indicates that hydroperoxyl (•OOH) and hydroxyl (•OH) radicals can be produced over 365-nm-irradiated BN/TiO_2 and TiO_2 alone via photoexcited electrons reducing dissolved O_2 and holes oxidizing water and direct oxidation of PFOA via photogenerated holes is thermodynamically favorable. Over BN alone, however, no ROS species can be formed since BN cannot be photoexcited by 365-nm light. To detect radical formation over BN/TiO_2, we performed BMPO spin-trapping EPR measurements [68]. (Fig. 8a,c). BN/TiO_2 displayed a more intense hydroxyl radical EPR spectrum compared to TiO_2, qualitatively indicating the formation of more hydroxyl radicals, consistent with the hypothesis of improved charge carrier separation contributing to more holes oxidizing H_2O to form •OH.

Adding *tert*-butanol (TBA), a commonly used hydroxyl radical scavenger, to the BN/TiO_2 system quenched the hydroxyl radical signals. Adding EDTA-2Na, a hole scavenger, also quenched the hydroxyl radical signals, which is consistent with •OH being produced from hole oxidation of water and not from decomposition of H_2O_2 which could be generated from reduction of O_2 with photoexcited e⁻s. Similar results were found using 254-nm light (Fig. 8c,d). We conclude that enhanced •OH formation results from the improved electron-hole pair separation from the BN/TiO_2 heterojunction. We expect this improved charge separation to also favor hole oxidation of PFOA, since water and PFOA oxidation potentials are similarly close to the VB level of hole-containing BN (Fig. 6).

We assessed the sensitivity of BN/TiO_2-photocatalyzed degradation of PFOA to the presence of scavenging agents, including TBA (for •OH), superoxide dismutase (SOD, for •HO_2), and EDTA-2Na (for h⁺). All inhibited PFOA oxidation, with EDTA-2Na being the most effective. TBA (which quenched the •OH EPR signals completely) caused $\sim 5\%$ PFOA to degrade after 120 min under 365-nm light and 60 min under 254-nm light (Fig. 8b,d). The involvement of these three oxidative species is consistent with reaction mechanisms previously suggested by us and other researchers. We propose that PFOA and short chain PFCAs adsorb to the hydrophobic BN surface and reacts with a photogenerated hole to

form a perfluoroalkyl radical, followed by Kolbe decarboxylation, HF elimination, and oxidation steps that lead to ever-shortening PFCA reaction intermediates [31,33,68,69].

4. Practical implications

4.1. Energy efficiency of BN/TiO_2 photocatalysts

We calculated the fluence dose in the units of J/cm^2, which has not been reported for other photocatalytic PFOA (or PFAS) degradation systems [70]. Reporting degradation performance in terms of fluence dose allows for systems-level comparisons of UV-based treatment studies [71]. In our light reactor system, ~ 4–$8 \, J/cm^2$ is required to degrade $\sim 120 \, \mu M$ PFOA in the $UV/BN/TiO_2$ system to undetectable levels (Fig. 3a and S5a). For comparison, typical commercial UV/H_2O_2-based processes for other contaminants use fluence doses below $2 \, J/cm^2$, which reflects the known difficulty in decomposing PFOA [72].

To establish a baseline for water treatment costs, we calculated an electrical energy per order (EE/O), which is defined as the number of kilowatts-hour (kWh) of electrical energy required to remove the concentration of a pollutant (*i.e.*, PFOA) by one order of magnitude (90%) in one cubic meter of contaminated water (Equation (3) and Text S5).

$$EE/O(kWh/m^3/order) = \frac{P \times \left(\frac{t}{60}\right)}{V \times \log\left(\frac{C_0}{C}\right)} \tag{3}$$

where V is the reaction volume (m^3), C and C_0 are concentrations of PFOA at some time t and at $t = 0$ min. We note that there are differing ways to calculate EE/O, depending on how P is defined. Current literature shows P defined as the total power based on the power input to the lamp [73–75], the output of the lamp [76,77], or the power reaching the reaction volume determined by chemical actinometry[78]. As researchers commonly use the lamp output in their calculations (Table S4), we calculated EE/O values (labeled EE/O_{output}) using the total lamp output for literature comparison. The BN/TiO_2 composite had EE/O_{output} values of 102 and 253 kWh/m^3/order using 254-nm and 365-nm light, respectively (Table S4). These are $> 10 \times$ smaller than the corresponding values for TiO_2 (1347 and 3620 kWh/m^3/order, respectively). The EE/O_{output} of BN (under UVC) was 116 kWh/m^3/order, also $> 10 \times$ smaller than that for TiO_2. Acknowledging the differences in reactor geometry, we note the EE/O_{output} for BN/TiO_2 under UVC falls within the wide range of reported values (Table S4).

In addition to EE/O_{output}, we calculated the EE/O based on chemical actinometry-based power (labeled EE/O_{CA}). EE/O_{CA} represents the minimum power needed to reach one order of magnitude removal, which presumes perfect transmission of electricity from the electrical source to the lamp, no energy loss in photon conversion, and no photon loss from the lamp into the reactor volume. The BN/TiO_2 composite had EE/O_{CA} values of 6.5 and 3.8 kWh/m^3/order under 254-nm and 365-nm, respectively, which are $< 10 \times$ smaller than the corresponding values for TiO_2 (85.9 and 54.3 kWh/m^3/order, respectively). BN had an EE/O_{CA} value of 7.4 kWh/m^3/order with UVC. The large differences in EE/O_{output} and EE/O_{CA} indicate improved photoreactor design and light delivery for BN/TiO_2 (as well as BN) can substantially lower EE/O_{output} values. An EE/O_{output} range of < 0.5 to 10 kWh/m^3 is considered cost competitive for water treatment [79].

4.2. Reusing BN/TiO_2

Full-scale photocatalyst slurry reactors continuously recirculate and separate (*i.e.*, using in-line ceramic membranes [80]) photocatalytic materials as a powder suspension. Towards potential use in such a system, we examined the reusability and stability of BN/TiO_2 by adding additional PFOA each time the initial PFOA was degraded to a non-detectable level (see Tables S5 and S6 for experimental details). BN/TiO_2 maintained activity for at least 4 cycles of PFOA degradation
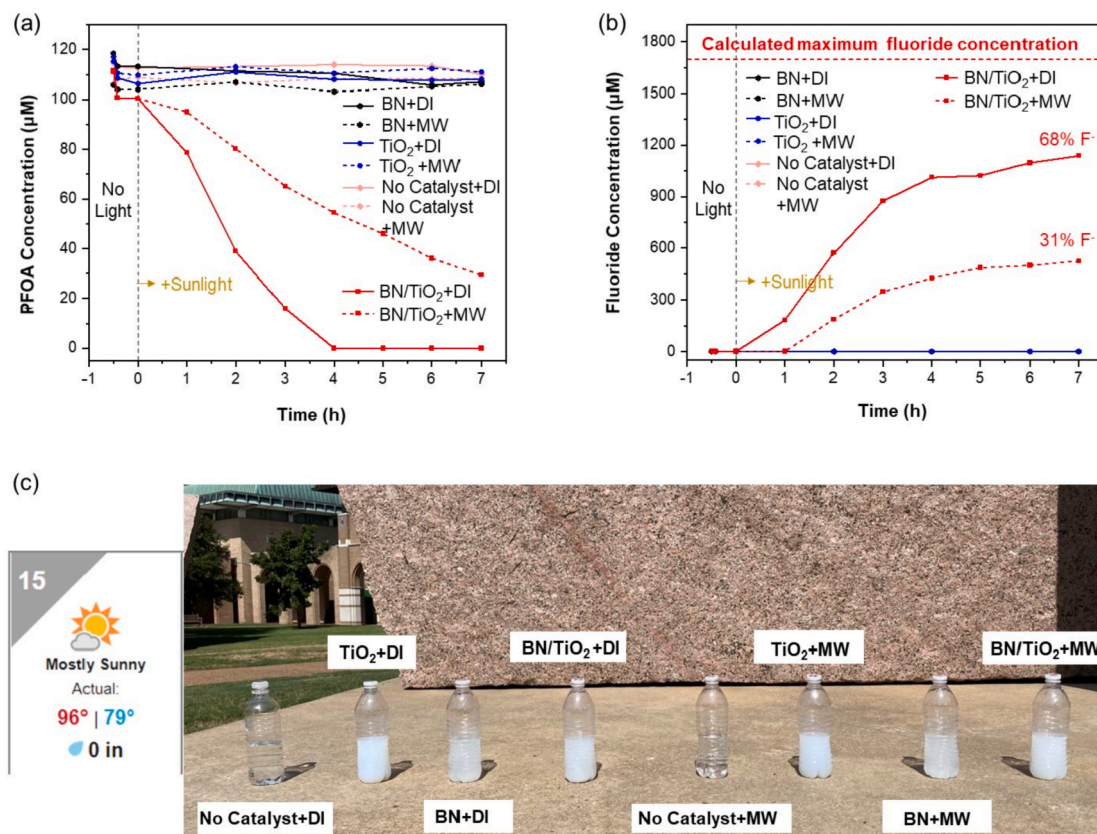
Fig. 9. (a) PFOA concentration−time profiles under natural sunlight with DI water and MW. (b) The released fluoride concentration profiles under the natural sunlight irradiation. (c) Weather conditions and photographic image of the outdoor sunlight experiment. Reaction conditions: [PFOA] (at t = ∼ −0.5 h) = ∼120 μM (50 ppm), catalyst dosage of 0.5 g/L, temperature: 79–96 °F (26–36 °C), air headspace, unstirred, sealed plastic water bottle, natural sunlight, the spectral irradiance of solar irradiation is ∼ 85 mW/cm^2.

(Figure S6). We found up to 70% total defluorination after 4 cycles of UV-A treatment, and 75% total defluorination after 5 cycles of UV-C treatment. The BN/TiO$_2$ composite showed no decrease in photocatalytic activity during UV- light irradiation, which is essential for full-scale continuous flow operation.

4.3. BN/TiO$_2$ degrades PFOA using natural sunlight

Sunlight provides a source of UV radiation; ∼95% of solar UV rays that reach earth are UV-A, with UV-B comprising the remaining 5% [81]. Solar disinfection in remote, off-grid locations rely upon UV and thermal radiation in sunlight to treat contaminated water using transparent containers [82]. This water treatment method has been used worldwide, especially in low-income and developing countries because of insufficient/improper/lack of wastewater treatment plants [83].

We carried out PFOA degradation in conventional plastic water bottles (no quartz flask reactors, no magnetic stirring or agitation), and in DI water and in salt-containing model water (MW). The corresponding UV–vis spectrum of the plastic water bottle (Figure S7) demonstrated light absorbance in the UV range as expected. The model water has a salt composition profile (11 mM total salts, ionic strength of 8.5 mM) typical of drinking water (Table S7). BN/TiO$_2$ showed significant PFOA degradation using outdoor sunlight; neither BN nor TiO$_2$ were active (Fig. 9). The PFOA concentration decreased from ∼ 100 μM (t = 0 h) to nondetectable levels (<2.4 μM) in DI water after 4 h ($t_{1/2}$ = 1.7 h); total defluorination was 60% at 4 h and 68% at 7 h. PFOA degradation was slower when the model water was used ($t_{1/2}$ = 4.5 h). The PFOA concentration decreased to 30 μM, and total defluorination increased to 31% after 7 h of sunlight exposure. Overall, these results point to exciting possibilities for BN/TiO$_2$ as an effective PFAS photocatalyst

with further development, unrestricted to UV-C wavelengths.

5. Conclusions

In this study, we synthesized a BN/TiO$_2$ composite photocatalyst through a simple calcination procedure. XPS analysis confirmed chemical bond formation between the BN plates and TiO$_2$ nanoparticles. The composite had excellent PFOA photodegradation capabilities under both UV-A light, where TiO$_2$ alone was only slightly active and BN alone was inactive.UPS and DR-UV analyses confirmed that BN/TiO$_2$ is a type II heterojunction with improved charge separation due to photogenerated hole migration to the BN domains. Photogenerated holes played a were critical to PFOA degradation as shown by EPR results and radical scavenging experiments. The composite was shown to be active for multiple cycles of PFOA degradation without deactivatio, and was demonstrated to be able to treat model water spiked with PFOA in conventional plastic bottles under actual sunlight.

Declaration of Competing Interest

The authors declare that they have no known competing financial interests or personal relationships that could have appeared to influence the work reported in this paper.

Data availability

Data will be made available on request.

Acknowledgments

Appendix A. Supplementary data

Supporting information is available online, including details of materials and methods, XRD spectra, HR-TEM, SEM and elemental mapping, XPS, and BET surface areas of materials, catalyst dosage photocatalytic experiments, chemical actinometry experiments, and EE/O calculations. Supplementary data to this article can be found online at https://doi.org/10.1016/j.cej.2022.137735.

References

[1] J. Cui, P. Gao, Y. Deng, Destruction of per- and polyfluoroalkyl substances (PFAS) with advanced reduction processes (ARPs): A critical review, Environ. Sci. Technol. 54 (2020) 3752–3766.

[2] R.K. Singh, S. Fernando, S.F. Baygi, N. Multari, S.M. Thagard, T.M. Holsen, Breakdown products from perfluorinated alkyl substances (PFAS) degradation in a plasma-based water treatment process, Environ. Sci. Technol. 53 (5) (2019) 2731–2738.

[3] Y. Li, T. Fletcher, D. Mucs, K. Scott, C.H. Lindh, P. Tallving, K. Jakobsson, Half-lives of PFOS, PFHxS and PFOA after end of exposure to contaminated drinking water, Occup. Environ. Med. 75 (1) (2018) 46–51.

[4] Y. Pan, Y. Zhu, T. Zheng, Q. Cui, S.L. Buka, B. Zhang, Y. Guo, W. Xia, L. Yeung, Y. Li, Novel chlorinated polyfluorinated ether sulfonates and legacy per-/ polyfluoroalkyl substances: placental transfer and relationship with serum albumin and glomerular filtration rate, Environ. Sci. Technol. 51 (2017) 634–644.

[5] M.S. Shimizu, R. Mott, A. Potter, J. Zhou, K. Baumann, J.D. Surratt, B. Turpin, G. B. Avery, J. Harfmann, R.J. Kieber, R.N. Mead, S.A. Skrabal, J.D. Willey, Atmospheric deposition and annual flux of legacy perfluoroalkyl substances and replacement perfluoroalkyl ether carboxylic acids in Wilmington, NC, USA, Environ. Sci. Technol. Lett. 8 (2021) 366–372.

[6] PFAS are ubiquitous in rainwater, C\&EN Glob, Enterp. 99 (2021) 6, https://doi. org/10.1021/cen-09913-scicon2.

[7] K.A. Barzen-Hanson, S.C. Roberts, S. Choyke, K. Oetjen, A. McAlees, N. Riddell, R. McCrindle, P.L. Ferguson, C.P. Higgins, J.A. Field, Discovery of 40 classes of per- and polyfluoroalkyl substances in historical aqueous film-forming foams (AFFFs) and AFFF-impacted groundwater, Environ. Sci. Technol. 51 (4) (2017) 2047–2057.

[8] A. Baabish, S. Sobhanei, H. Fiedler, Priority perfluoroalkyl substances in surface waters-A snapshot survey from 22 developing countries, Chemosphere 273 (2021), 129612.

[9] A.M. Ali, C.P. Higgins, W.M. Alarif, S.S. Al-Lihaibi, M. Ghandourah, R. Kallenborn, Per-and polyfluoroalkyl substances (PFASs) in contaminated coastal marine waters of the Saudi Arabian Red Sea: a baseline study, Environ. Sci. Pollut. Res. 28 (3) (2021) 2791–2803.

[10] J.C. Baluyot, E.M. Reyes, M.C. Velarde, Per-and polyfluoroalkyl Substances (PFAS) as Contaminants of Emerging Concern in Asia's Freshwater Resources, Environ. Res. 197 (2021) 111122.

[11] L.W.Y. Yeung, C. Dassuncao, S. Mabury, E.M. Sunderland, X. Zhang, R. Lohmann, Vertical Profiles, Sources, and Transport of PFASs in the Arctic Ocean, Env. Sci Technol. 51 (2017) 6735–6744.

[12] B.J. Place, J.A. Field, Identification of novel fluorochemicals in aqueous film-forming foams used by the US military, Environ. Sci. Technol. 46 (13) (2012) 7120–7127.

[13] J.R. Masoner, D.W. Kolpin, I.M. Cozzarelli, K.L. Smalling, S.C. Bolyard, J.A. Field, E.T. Furlong, J.L. Gray, D. Reinhart, A. Rodowa, P.M. Bradley, Landfill leachate contributes per-/poly-fluoroalkyl substances (PFAS) and pharmaceuticals to municipal wastewater, Environ. Sci. Water Res. Technol. 6 (5) (2020) 1300–1311.

[14] P. Jacob, K.A. Barzen-Hanson, D.E. Helbling, Target and Nontarget Analysis of Per-and Polyfluoralkyl Substances in Wastewater from Electronics Fabrication Facilities, Environ. Sci. Technol. 55 (4) (2021) 2346–2356.

[15] O.S. Arvaniti, A.S. Stasinakis, Review on the occurrence, fate and removal of perfluorinated compounds during wastewater treatment, Sci. Total Environ. 524 (2015) 81–92.

[16] Z. Du, S. Deng, Y. Chen, B. Wang, J. Huang, Y. Wang, G. Yu, Removal of perfluorinated carboxylates from washing wastewater of perfluorooctanesulfonyl fluoride using activated carbons and resins, J. Hazard. Mater. 286 (2015) 136–143.

[17] C.Y. Tang, Q.S. Fu, A.P. Robertson, C.S. Criddle, J.O. Leckie, Use of reverse osmosis membranes to remove perfluorooctane sulfonate (PFOS) from semiconductor wastewater, Environ. Sci. Technol. 40 (23) (2006) 7343–7349.

[18] S. Deng, Q. Yu, J. Huang, G. Yu, Removal of perfluorooctane sulfonate from wastewater by anion exchange resins: Effects of resin properties and solution chemistry, Water Res. 44 (2010) 5188–5195.

[19] U.S. Epa, EPA Announces Plans for New Wastewater Regulations, Including First Limits for PFAS, Updated Limits for Nutrients, 2020 https://www.epa.gov/ newsreleases/epa-announces-plans-new-wastewater-regulations-including-first-limits-pfas-updated.

[20] S.C. Panchangam, A.-C. Lin, K.L. Shaik, C.-F. Lin, Decomposition of perfluorocarboxylic acids (PFCAs) by heterogeneous photocatalysis in acidic aqueous medium, Chemosphere 77 (2) (2009) 242–248.

[21] Y. Zhu, T. Xu, D. Zhao, F. Li, W. Liu, B. Wang, B. An, Adsorption and solid-phase photocatalytic degradation of perfluorooctane sulfonate in water using gallium-doped carbon-modified titanate nanotubes, Chem. Eng. J. 421 (2021), 129676.

[22] B. Gomez-Ruiz, P. Ribao, N. Diban, M.J. Rivero, I. Ortiz, A. Urtiaga, Photocatalytic degradation and mineralization of perfluorooctanoic acid (PFOA) using a composite TiO2– rGO catalyst, J. Hazard. Mater. 344 (2018) 950–957.

[23] M. Li, Z. Yu, Q. Liu, L. Sun, W. Huang, Photocatalytic decomposition of perfluorooctanoic acid by noble metallic nanoparticles modified TiO2, Chem. Eng. J. 286 (2016) 232–238.

[24] A. Tian, Y. Wu, K. Mao, Enhanced performance of surface modified TiO2 nanotubes for the decomposition of perfluorooctanoic acid, 1802 (2017) 20029. https://doi. org/10.1063/1.4971911.

[25] Y. Sun, G. Li, W. Wang, W. Gu, P.K. Wong, T. An, Photocatalytic defluorination of perfluorooctanoic acid by surface defective BiOCl: Fast microwave solvothermal synthesis and photocatalytic mechanisms, J. Environ. Sci. 84 (2019) 69–79.

[26] T. Li, C. Wang, T. Wang, L. Zhu, Highly efficient photocatalytic degradation toward perfluorooctanoic acid by bromine doped BiOI with high exposure of (001) facet, Appl. Catal. B Environ. 268 (2020), 118442.

[27] S.P. Sahu, M. Qanbarzadeh, M. Ateia, H. Torkzadeh, A.S. Maroli, E.L. Cates, Rapid degradation and mineralization of perfluorooctanoic acid by a new petitjeanite Bi3O (OH)(PO4) 2 microparticle ultraviolet photocatalyst, Environ. Sci. Technol. Lett. 5 (8) (2018) 533–538.

[28] M. Qanbarzadeh, D. Wang, M. Ateia, S.P. Sahu, E.L. Cates, Impacts of Reactor Configuration, Degradation Mechanisms, and Water Matrices on Perfluorocarboxylic Acid Treatment Efficiency by the UV/Bi3O(OH)(PO4)2 Photocatalytic Process, ACS ES&T Eng. 1 (2020) 239–248.

[29] D. Huang, L. Yin, J. Niu, Photoinduced hydrodefluorination mechanisms of perfluorooctanoic acid by the SiC/Graphene catalyst, Environ. Sci. Technol. 50 (11) (2016) 5857–5863.

[30] B. Zhao, P. Zhang, Photocatalytic decomposition of perfluorooctanoic acid with β-Ga2O3 wide bandgap photocatalyst, Catal. Commun. 10 (2009) 1184–1187.

[31] X. Li, P. Zhang, L. Jin, T. Shao, Z. Li, J. Cao, Efficient photocatalytic decomposition of perfluorooctanoic acid by indium oxide and its mechanism, Environ. Sci. Technol. 46 (10) (2012) 5528–5534.

[32] Z. Li, P. Zhang, T. Shao, J. Wang, L. Jin, X. Li, Different nanostructured In2O3 for photocatalytic decomposition of perfluorooctanoic acid (PFOA), J. Hazard. Mater. 260 (2013) 40–46.

[33] L. Duan, B. Wang, K. Heck, S. Guo, C.A. Clark, J. Arredondo, M. Wang, T.P. Senftle, P. Westerhoff, X. Wen, Y. Song, M.S. Wong, Efficient photocatalytic PFOA degradation over boron nitride, Environ. Sci. Technol. Lett. 7 (8) (2020) 613–619.

[34] M. Kim, A. Peeples, H. Estrada, S. Fowler, L. Chiang, J. Morgan, M. Doganay, B. Walls, B. Wang, J.C. Samba, Destruction of Per-and Polyfluoroalkyl Substances using UVC and Boron Nitride, in: 2021 Waste-Management Educ. Res. Conf., IEEE, 2021: pp. 1–7.

[35] Y. Kimura, T. Wakabayashi, T. Okada, T. Wada, H. Nishikawa, Boron nitride as a lubricant additive, Wear 232 (2) (1999) 199–206.

[36] G. Cassabois, P. Valvin, B. Gil, Hexagonal boron nitride is an indirect bandgap semiconductor, Nat. Photonics. 10 (4) (2016) 262–266.

[37] P. Westerhoff, P.J.J. Alvarez, J. Kim, Q. Li, A. Alabastri, N.J. Halas, D. Villagran, J. Zimmerman, M.S. Wong, Utilizing the broad electromagnetic spectrum and unique nanoscale properties for chemical-free water treatment, Curr. Opin. Chem. Eng. 33 (2021), 100709.

[38] S.C. Bolyard, A.M. Motlagh, D. Lozinski, D.R. Reinhart, Impact of organic matter from leachate discharged to wastewater treatment plants on effluent quality and UV disinfection, Waste Manag. 88 (2019) 257–267.

[39] J. Wang, C. Cao, Y. Wang, Y. Wang, B. Sun, L. Zhu, In situ preparation of pn BiOI@ Bi5O7I heterojunction for enhanced PFOA photocatalytic degradation under simulated solar light irradiation, Chem. Eng. J. 391 (2020), 123530.

[40] Y. Wu, Y. Li, C. Fang, C. Li, Highly Efficient Degradation of Perfluorooctanoic Acid over a MnOx-Modified Oxygen-Vacancy-Rich In2O3 Photocatalyst, ChemCatChem 11 (9) (2019) 2297–2303.

[41] J. Gu, J. Yan, Z. Chen, H. Ji, Y. Song, Y. Fan, H. Xu, H. Li, Construction and preparation of novel 2D metal-free few-layer BN modified graphene-like g-C3N4 with enhanced photocatalytic performance, Dalt. Trans. 46 (34) (2017) 11250–11258.

[42] B. Singh, G. kaur, P. Singh, K. Singh, J. Sharma, M. Kumar, R. Bala, R. Meena, S. K. Sharma, A. Kumar, Nanostructured BN–TiO2 composite with ultra-high photocatalytic activity, New J. Chem. 41 (20) (2017) 11640–11646.

[43] D. Liu, D. Zhang, W. Xie, L.u. Sun, Y. Chen, W. Lei, Porous BN/TiO2 hybrid nanosheets as highly efficient visible-light-driven photocatalysts, Appl. Catal. B 207 (2017) 72–78.

[44] Q. Li, X. Hou, Z. Fang, T. Yang, J. Chen, X. Cui, T. Liang, J. Shi, Construction of layered h-BN/TiO2 hetero-structure and probing of the synergetic photocatalytic effect, Sci. China Mater. 63 (2) (2020) 276–287.

[45] L. Dong, W. Cui, L. Jing, Y. Xue, C. Tang, A novel TiO2 xNx/BN composite photocatalyst: Synthesis, characterization and enhanced photocatalytic activity for Rhodamine B degradation under visible light, Catal. Commun. 57 (2014) 9–13.

[46] Y. Sheng, J. Yang, F. Wang, L. Liu, H.u. Liu, C. Yan, Z. Guo, Jie, Yang, Fang, Wang, Lichun, Liu, Hu, Sol-gel synthesized hexagonal boron nitride/titania nanocomposites with enhanced photocatalytic activity, Appl. Surf. Sci. 465 (2019) 154–163.

[47] M. Nasr, R. Viter, C. Eid, R. Habchi, P. Miele, M. Bechelany, Enhanced photocatalytic performance of novel electrospun BN/TiO2 composite nanofibers, New J. Chem. 41 (2017) 81–89.

[48] C. Byrne, S. Rhatigan, D. Hermosilla, N. Merayo, Á. Blanco, M.C. Michel, S. Hinder, M. Nolan, S.C. Pillai, Modification of TiO2 with hBN: high temperature anatase phase stabilisation and photocatalytic degradation of 1, 4-dioxane, J. Phys. Mater. 3 (2019) 15009.

[49] L. Lin, W. Jiang, M. Bechelany, M. Nasr, J. Jarvis, T. Schaub, R.R. Sapkota, P. Miele, H. Wang, P. Xu, Adsorption and photocatalytic oxidation of ibuprofen using nanocomposites of TiO2 nanofibers combined with BN nanosheets: Degradation products and mechanisms, Chemosphere 220 (2019) 921–929.

[50] Y. Liu, W. Miao, X. Fang, Y. Tang, S. Mao, MOF-derived metal-free N-doped porous carbon mediated peroxydisulfate activation via radical and non-radical pathways: Role of graphitic N and C O, Chem. Eng. J. 380 (2019), 122584.

[51] Y. Feng, J. Zhu, J. Jiang, W. Wang, G. Meng, F. Wu, Y. Gao, X. Huang, Building smart TiO2 nanorod networks in/on the film of P25 nanoparticles for high-efficiency dye sensitized solar cells, Rsc Adv. 4 (25) (2014) 12944–12949.

[52] M. Jalaly, F. José Gotor, M. Semnan, M., Jesús Sayagués, A novel, simple and rapid route to the synthesis of boron cabonitride nanosheets: combustive gaseous unfolding, Rep. 7 (2017) 3453.

[53] W. Yang, H. Shen, H. Min, J. Ge, Enhanced visible light-driven photodegradation of rhodamine B by Ti3+ self-doped TiO2@Ag nanoparticles prepared using Ti vapor annealing, J. Mater. Sci. 55 (2) (2020) 701–712.

[54] F.P. Larkins, A. Lubenfeld, The Auger spectrum of solid ammonia, J. Electron Spectros. Relat. Phenomena. 15 (1) (1979) 137–144.

[55] M. Datta, H.J. Mathieu, D. Landolt, Characterization of transpassive films on nickel by sputter profiling and angle resolved AES/XPS, Appl. Surf. Sci. 18 (1984) 299–314.

[56] G. Liu, Y. Zhao, C. Sun, F. Li, G. Lu, H.-M. Cheng, Synergistic effects of B/N doping on the visible-light photocatalytic activity of mesoporous TiO2, Angew. Chemie Int. Ed. 47 (24) (2008) 4516–4520.

[57] B.R. Strohmeier, Surface characterization of aluminum foil annealed in the presence of ammonium fluoborate, Appl. Surf. Sci. 40 (3) (1989) 249–263.

[58] Y. Yang, W. Ji, X. Li, Z. Zheng, F. Bi, M. Yang, J. Xu, X. Zhang, Insights into the degradation mechanism of perfluorooctanoic acid under visible-light irradiation through fabricating flower-shaped Bi5O7I/ZnO nn heterojunction microspheres, Chem. Eng. J. 420 (2021), 129934.

[59] T. Yamada, T. Masuzawa, T. Ebisudani, K. Okano, T. Taniguchi, Field emission characteristics from graphene on hexagonal boron nitride, Appl. Phys. Lett. 104 (2014), 221603.

[60] E. Han, K. Vijayarangamuthu, J. Youn, Y.-K. Park, S.-C. Jung, K.-J. Jeon, Degussa P25 TiO2 modified with H2O2 under microwave treatment to enhance photocatalytic properties, Catal. Today. 303 (2018) 305–312.

[61] J. Schneider, M. Matsuoka, M. Takeuchi, J. Zhang, Y. Horiuchi, M. Anpo, D. W. Bahnemann, Understanding TiO2 photocatalysis: mechanisms and materials, Chem. Rev. 114 (2014) 9919–9986.

[62] Y. Nosaka, A.Y. Nosaka, Generation and detection of reactive oxygen species in photocatalysis, Chem. Rev. 117 (17) (2017) 11302–11336.

[63] Y. Chen, M. Bhati, B.W. Walls, B. Wang, M.S. Wong, T.P. Senftle, Mechanistic Insight into the Photo-Oxidation of Perfluorocarboxylic Acid over Boron Nitride, Env, Sci Technol. 56 (12) (2022) 8942–8952.

[64] J. Low, J. Yu, M. Jaroniec, S. Wageh, A.A. Al-Ghamdi, Heterojunction photocatalysts, Adv. Mater. 29 (2017) 1601694.

[65] H. Wang, L. Zhang, Z. Chen, J. Hu, S. Li, Z. Wang, J. Liu, X. Wang, Semiconductor heterojunction photocatalysts: design, construction, and photocatalytic performances, Chem. Soc. Rev. 43 (2014) 5234–5244.

[66] K. Li, X. Lu, Y. Zhang, K. Liu, Y. Huang, H. Liu, Bi3TaO7/Ti3C2 heterojunctions for enhanced photocatalytic removal of water-borne contaminants, Environ. Res. 185 (2020), 109409.

[67] X. Zhao, Y. You, S. Huang, Y. Wu, Y. Ma, G. Zhang, Z. Zhang, Z-scheme photocatalytic production of hydrogen peroxide over Bi4O5Br 2/g-C3N4 heterostructure under visible light, Appl. Catal. B Environ. 278 (2020), 119251.

[68] H. Javed, J. Metz, T.C. Eraslan, J. Mathieu, B.o. Wang, G. Wu, A.-L. Tsai, M. S. Wong, P.J.J. Alvarez, Discerning the Relevance of Superoxide in PFOA Degradation, Environ. Sci. Technol. Lett. 7 (9) (2020) 653–658.

[69] J. Wang, C. Cao, Y. Zhang, Y. Zhang, L. Zhu, Underneath mechanisms into the super effective degradation of PFOA by BiOF nanosheets with tunable oxygen vacancies on exposed (101) facets, Appl. Catal. B Environ. 286 (2021), 119911.

[70] H.O. Tugaoen, P. Herckes, K. Hristovski, P. Westerhoff, Influence of ultraviolet wavelengths on kinetics and selectivity for N-gases during TiO2 photocatalytic reduction of nitrate, Appl. Catal. B Environ. 220 (2018) 597–606.

[71] S. Sanches, M.T. Barreto Crespo, V.J. Pereira, Drinking water treatment of priority pesticides using low pressure UV photolysis and advanced oxidation processes, Water Res. 44 (6) (2010) 1809–1818.

[72] S.R. Sarathy, M.I. Stefan, A. Royce, M. Mohseni, Pilot-scale UV/H2O2 advanced oxidation process for surface water treatment and downstream biological treatment: effects on natural organic matter characteristics and DBP formation potential, Environ. Technol. 32 (2011) 1709–1718.

[73] J. Ye, J. Liu, C. Li, P. Zhou, S. Wu, H. Ou, Heterogeneous photocatalysis of tris (2-chloroethyl) phosphate by UV/TiO2: degradation products and impacts on bacterial proteome, Water Res. 124 (2017) 29–38.

[74] F. Rehman, M. Sayed, J.A. Khan, N.S. Shah, H.M. Khan, D.D. Dionysiou, Oxidative removal of brilliant green by UV/S2O82-, UV/HSO5-and UV/H2O2 processes in aqueous media: a comparative study, J. Hazard. Mater. 357 (2018) 506–514.

[75] S. Satyro, M. Race, R. Marotta, M. Dezotti, D. Spasiano, G. Mancini, M. Fabbricino, Simulated solar photocatalytic processes for the simultaneous removal of EDDS, Cu (II), Fe (III) and Zn (II) in synthetic and real contaminated soil washing solutions, J. Environ. Chem. Eng. 2 (4) (2014) 1969–1979.

[76] N. Helaïli, Y. Bessekhouad, A. Bouguelia, M. Trari, p-Cu2O/n-ZnO heterojunction applied to visible light Orange II degradation, Sol. Energy. 84 (7) (2010) 1187–1192.

[77] S. Lu, G. Meng, C. Wang, H. Chen, Photocatalytic inactivation of airborne bacteria in a polyurethane foam reactor loaded with a hybrid of MXene and anatase TiO2 exposing 0 0 1 facets, Chem. Eng. J. 404 (2021), 126526.

[78] H. Javed, C. Lyu, R. Sun, D. Zhang, P.J.J. Alvarez, Discerning the inefficacy of hydroxyl radicals during perfluorooctanoic acid degradation, Chemosphere 247 (2020), 125883.

[79] S.K. Loeb, P.J.J. Alvarez, J.A. Brame, E.L. Cates, W. Choi, J. Crittenden, D. D. Dionysiou, Q. Li, G. Li-Puma, X. Quan, D.L. Sedlak, T. David Waite, P. Westerhoff, J.-H. Kim, The Technology Horizon for Photocatalytic Water Treatment: Sunrise or Sunset? Environ. Sci. Technol. 53 (6) (2019) 2937–2947.

[80] H.O. Stancl, K. Hristovski, P. Westerhoff, Hexavalent chromium removal using UV-TiO2/ceramic membrane reactor, Environ. Eng. Sci. 32 (8) (2015) 676–683.

[81] T.G. Polefka, T.A. Meyer, P.P. Agin, R.J. Bianchini, Effects of solar radiation on the skin, J. Cosmet. Dermatol. 11 (2012) 134–143.

[82] K.G. McGuigan, R.M. Conroy, H.-J. Mosler, M. du Preez, E. Ubomba-Jaswa, P. Fernandez-Ibanez, Solar water disinfection (SODIS): a review from bench-top to roof-top, J. Hazard. Mater. 235 (2012) 29–46.

[83] S.M. Parsa, S. Momeni, A. Hemmat, M. Afrand, Effectiveness of solar water disinfection in the era of COVID-19 (SARS-CoV-2) pandemic for contaminated water/wastewater treatment considering UV effect and temperature, J. Water Process Eng. 43 (2021), 102224.